uc3m | Universidad Carlos III de Madrid

e-Archivo

This is a postprint version of the following published document:

Galindo-Romera, G., Herraiz-Martínez, F. J., Gil, M., Martínez-Martínez, J. J., & Segovia-Vargas, D. (2016). Submersible Printed Split-Ring Resonator-Based Sensor for Thin-Film Detection and Permittivity Characterization. IEEE Sensors Journal, 16(10), 3587–3596.

DOI: 10.1109/JSEN.2016.2538086

© 2016 IEEE. Personal use of this material is permitted. Permission from IEEE must be obtained for all other uses, in any current or future media, including reprinting/republishing this material for advertising or promotional purposes, creating new collective works, for resale or redistribution to servers or lists, or reuse of any copyrighted component of this work in other works.

Submersible Printed Split-Ring Resonator-Based Sensor for Thin-Film Detection and Permittivity Characterization

Gabriel Galindo-Romera, Francisco Javier Herraiz-Martínez, *Member, IEEE*, Marta Gil, José Juan Martínez-Martínez, and Daniel Segovia-Vargas, *Member, IEEE*

***Abstract*— A Split-Ring Resonator (SRR) based sensor for the detection of solid thickness and relative permittivity characterization of solid and liquid materials is proposed. The structure is composed of two SRRs hosted in a microstrip transmission line. The sensing principle is based on the detection of the notch introduced by the resonators in the transmission coefficient. Hence, a frequency shift of the notch is related to a change in the effective permittivity of the structure when the sensor is covered with any solid or liquid material. A complete characterization of the sensor, for the three proposed applications, is performed through simulations. Finally, all simulated results are corroborated with measurements. The proposed sensor is implemented in single-layer printed technology, resulting in a low-cost and low-complexity solution. It presents real-time response and high sensitivity. Moreover, it is fully submersible and reusable.**

***Index Terms*— Effective permittivity, resonator, sensor, Split-Ring Resonator (SRR), submersible sensor.**

I. Introduction

In the last years a growing demand to obtain the relative permittivity of materials has been reported [1]-[3]. Several techniques based on the detection of the changes produced in the frequency response due to the presence of different materials have been found in the literature [4]-[9]. These techniques have been applied to different fields such as Biology or Chemistry among others [9]-[10], in the recent years. One of these emerging applications is the real-time detection and characterization of liquids. For instance, it would be useful a tool for genetic analysis [11] or the determination of the composition of different mixtures, such as ethanol and water [12]. Moreover, it is also interesting its application for sensing solids and their thickness [13]-[14].

The proposed approach performs these real-time analysis based on the frequency shift of electromagnetic resonators. In particular, the technology presented in this work is inspired on the planar Split-Ring Resonator (SRR). A SRR is composed of two concentric metallic rings with two gaps in opposite positions. The SRR was introduced by Pendry in late 90s [15].

Manuscript submitted 4 December 2015.

The authors are with the GREMA (Radiofrequency, Electromagnetism, Microwaves and Antennas Group), Carlos III University in Madrid, Leganés, Madrid 28045 Spain (e-mail: ggalindo@ tsc.uc3m.es).

Printed structures based on SRRs are becoming an interesting structure for sensing applications due to their low-cost, quick response time, high sensitivity and selectivity [16]-[20]. Specifically, these structures can be used to measure the complex permittivity of solids and liquids. This can be done by relating the resonant frequency of the SRRs to the real part of the permittivity of material under test (MUT). Moreover, SRRs are also useful for thickness detection of thin-films [21]-[23]. Up to now, SRRs have been used in the terahertz [21], mm-wave [22] and ten-gigahertz [23] bands for thin-film detection. In these works the detection range is below 50 μm. Up to the authors' knowledge, SRRs have not been used in the low-gigahertz band for thickness detection. This band allows the detection of films between 100 μm and 1 mm approximately, as it will be shown in this work. Thus, this new range of measurement can be useful for other applications.

Nowadays, there exist multiple techniques for permittivity characterization. They can be divided into two different groups: destructive and non-destructive methods. A destructive method destroys or modifies the sample after measuring it, while with a non-destructive method the sample is still available with the initial characteristics after doing the measurement. A typical destructive measurement is performed with chemicals, transmission lines or resonant cavities. For instance, the transmission line method is considered as destructive because a portion of the MUT has to be situated inside the transmission line, fitting particular dimensions. The same happens with the resonant cavity method, where a section of the MUT must be situated inside the cavity [2]. Within the non-destructive method different techniques can be found [2]-[3], as for example the coaxial probe method or the free space method, among others. The non-destructive methods are quicker and cheaper to implement and fabricate. Non-destructive sensors based on SRRs have become very popular due to their low-cost fabrication compared to other techniques. Moreover, they present quick response time and high sensitivity and selectivity.

Biological and chemical detection are one of the biggest applications of SRR-based sensors [9]-[10]. Some of liquid chemicals are dangerous for human health and, thus, its detection is crucial. In the most recent publications, microfluidic techniques have been added to SRR-based sensors [24]-[29]. The main idea is to conduct the liquid

through channels placed inside the most sensitive part of the SRR in order to detect a substance of interest. Nevertheless, up to the authors' knowledge electromagnetic submersible sensors have not been proposed until now. For some applications, it would be interesting to immerse the sensor directly in liquids without using microfluidic channels. Although microfluidics is a more complex technology than the proposed submersible sensor, the amount of needed liquid is tiny. This is an important fact in applications with a reduced amount of liquid sample, such as biological fluids sensing. On the other hand, in industrial applications, such as the measurement of oils and solvents, the amount of sample is large enough so a sensor can be directly submerged. It would reduce the complexity and cost fabrication. Moreover, the sensing of different liquids would be easier and quicker.

In the present work a printed electromagnetic sensor based on SRRs working below 2 GHz is presented. Thus, a fully planar and low-cost sensor is obtained. Firstly, it is suitable for the determination of the thickness of thin films situated over the sensor. Moreover, the proposed sensor can be used for the permittivity characterization of solid materials in real time and with a non-destructive approach. Finally, the electromagnetic sensing part is protected for liquids detection, obtaining a fully submersible and reusable sensor.

The organization of the paper is as follows: the proposed sensor and its working principle are presented in Section II; Section III shows the dielectric characterization of solids; the effect of the protection layer and the thin-layer detection and the dielectric characterization of liquids are presented in Section IV and Section V, respectively; finally, the paper is concluded in Section VI.

II. Split-Ring Resonator-Based Sensor and Working Principle

A. Split-Ring Resonator-based printed sensor

In this work, printed rectangular SRRs are used. The sketch of one printed rectangular SRR is shown Fig. 1 (a). The performance of rectangular SRR is the same than the circular SRR [30]. The structure is composed of two concentric metallic rings with two gaps in opposite positions. A magnetic field, perpendicular to the ring surface, applied over the structure will induce current through the rings. These currents go from one ring to the other one due to the distributed capacitance formed between them. The SRR can be modeled as a resonant LC structure (Fig. 1 (b)) [30], where *L* models the inductive behavior introduced by the conductive strips, while *C* models the distributed capacitance between the rings.

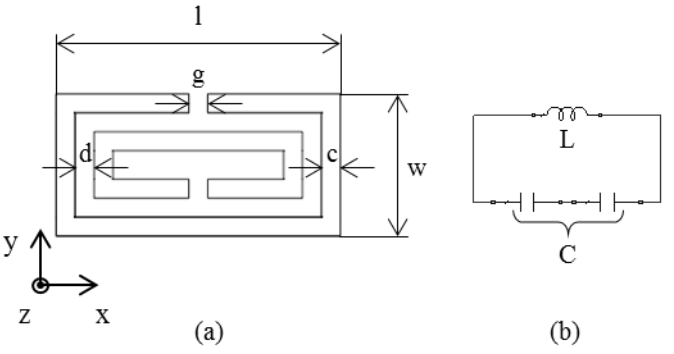

Fig. 1. Topology of the rectangular SRR (a) and its equivalent circuit (b).

Fig. 2 shows the top view of the proposed sensor (layout (a) and fabricated prototype (b)). It is implemented in microstrip technology. Microstrip technology is based on a metallization layer over a grounded dielectric substrate leading to printed single-layer microwave circuits [31]. The proposed sensor is composed of a transmission line loaded with two rectangular SRRs. The ends of the line are soldered to two SMA male connectors, acting as the ports of the sensor. The sensor is etched on the commercial dielectric substrate Rogers AD1000, with a relative dielectric constant of ε_r' = 10.6±0.35, loss tangent $tan\ \delta$ = 0.0023, substrate thickness h = 1.27 mm and a metallization thickness of 17 µm. The width of the microstrip line is W_l = 1.19 mm (designed to provide a 50-Ω characteristic impedance), the distance between the rings and between the rings and the microstrip line is d = 0.8 mm, the width of the gap is g = 0.8 mm and the width of the metallization of the rings is c = 0.8 mm. The length of the external ring is l = 12 mm and the width is w = 6 mm. Fig. 3 shows the simulated, with the software *ADS (Advanced Design System)* ®, and measured reflection and transmission coefficient results of the proposed sensor. The whole layout has been simulated. The simulation parameters are as follows: the simulator used is *Momentum Microwave*, the number of lines per wavelength is 20 and an adaptive frequency plan has been used. The Svensson-Djordjevic dispersive model is considered. The same simulation scheme has been used in all the full-wave simulations throughout the work. It can be seen that the resonant frequency is equal to 1.84 GHz in all cases, achieving good matching between simulation and experimental results. The dimensions of the sensor have been chosen in order to obtain a resonance frequency in the low-gigahertz band (below 2 GHz), because two of the goals of the work are the characterization of materials in the low-GHz band and the measurement of detection of films between 100 µm and 1 mm. The sensor can be easily escalated and, thus, re-designed in order to work in other frequency region. On the other hand, the implementation of two SRRs coupled to the microstrip line (Fig. 2) instead of just one has been considered because it improves the S parameters of the sensor, e. g. the notch is deeper in the transmission coefficient.

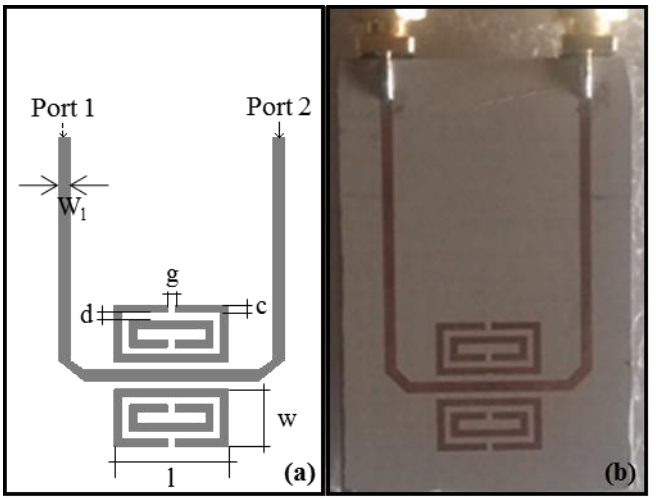

Fig. 2. Proposed sensor layout (a) and manufactured prototype (b).

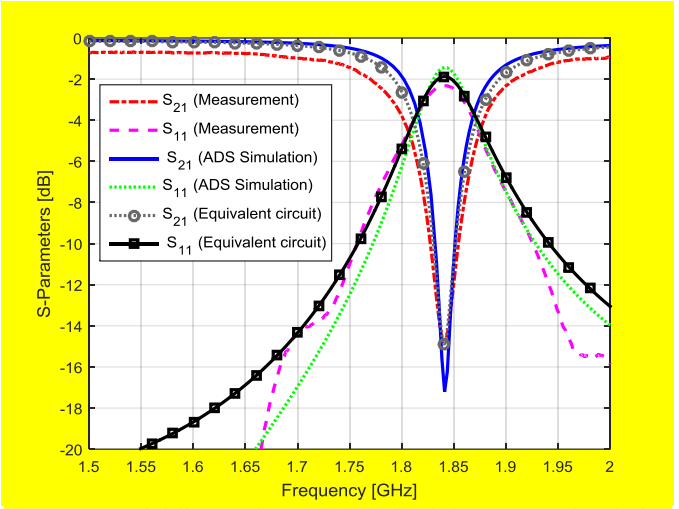

Fig. 3. Measured, full-wave electromagnetic simulation (ADS) and equivalent circuit model simulation S parameters of the proposed sensor.

B. *Sensing principle*

The SRRs introduce a notch in the transmission coefficient between the ports of the microstrip line due to the addition of a transmission pole. Thus, the working principle of the SRR-based sensor relies on the frequency shift of the notch that is produced when a material is situated over the SRRs. First of all, a quasi-TEM propagating mode is assumed due to the fact that the electric field lines in a microstrip line are not completely confined between the conductor strip and the ground plane. In microstrip line technology the guided wavelength is given by

$$\lambda_g = \frac{c_0}{f\sqrt{\varepsilon_{eff}}} \tag{1}$$

where c_0 is the speed of light in vacuum, ε_{eff} is the effective permittivity which takes into account that the electric field lines are not fully contained between the strip conductor and the ground plane. In the case of the proposed SRR-based structure ($c/h \leq 1$) the effective permittivity for the uncovered sensor is given by

$$\varepsilon_{eff} = \frac{\varepsilon_r + 1}{2} + \frac{\varepsilon_r - 1}{2}\left[\left(1 + 12(h/c)\right)^{-1/2} + 0.04\left(1 - (c/h)\right)^2\right] \tag{2}$$

Hence, if a material is situated over the structure, the fringing fields interact with the material and the characteristics of the line change [32]-[33]. An increase in the thickness of the material situated over the structure also increases the effective permittivity (ε_{eff}).

It can be deduced from the equivalent LC circuit that the resonant frequency (f_o) of a SRR can be obtained as

$$f_o = \frac{1}{2\pi}\sqrt{\frac{1}{LC}} \tag{3}$$

where L and C are the inductance and capacitance of the SRR, respectively, according to Fig. 1. Moreover, it can be seen that the capacitance and the inductance of SRR [30] follow the equations

$$C = \frac{\sqrt{\varepsilon_{eff}}}{c_0 Z_o}\frac{p_{int}}{4} \tag{4}$$

$$L = \frac{2\, p_{ext} Z_o \sqrt{\varepsilon_{eff}}}{c_0} \tag{5}$$

where Z_o is the characteristic impedance corresponding to a coplanar line formed between the inner and the exterior rings of the SRR [34], p_{int} is the perimeter defined by the gap between the rings, and p_{ext} is the perimeter defined by the external ring. It can be seen that the capacitance increases with increasing effective permittivity. Thus, an increased in the effective permittivity produces a decrease in the resonant frequency of the SRR.

Fig. 4 shows the equivalent circuit of the proposed sensor, where C_{SRR} and L_{SRR} take into account the capacitance and inductance of both SRRs. These values are computed as the parallel of two SRRs whose values are obtained from (4) and (5), as explained before. R_{loss} considers the metallization and dielectric losses of the printed SRRs and the dielectric losses when a sample is placed over the sensor. This term is used to characterize the imaginary part of the relative permittivity of the sample (ε_r'') and it is computed from the transmission coefficient of the circuit as:

$$R_{loss} = \frac{Z_o(1 - 10^{|S_{21}|/20})}{10^{|S_{21}|/20}} \cdot \frac{2}{2.95} \tag{6}$$

The lines of the equivalent circuit model represent the microstrip line of the sensor, each of them with half the total length of the sensor line. The other parameters of the lines (substrate and line width, W_l) are the same explained in

Section II.A. The values of the equivalent circuit model for the unloaded sensor are C_{SRR}=25.86 pF, L_{SRR}=0.30 nH and R_{loss}=442 Ω. Fig. 3 shows good agreement between the results of the equivalent circuit model and the measured and full-wave-simulation S parameters.

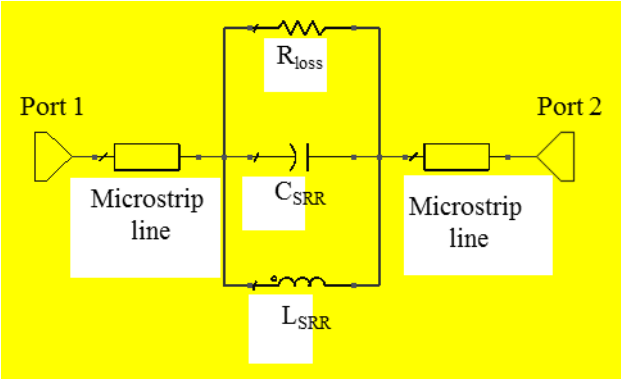

Fig. 4. Equivalent circuit model of the proposed sensor

In Fig. 5 the theory previously exposed is demonstrated through simulations. The sensor presented in Section II.A has been simulated in two different situations: the uncovered sensor and the covered one with a 3-mm-thickness material. The material has a permittivity ε'_{r2} = 5. In Fig. 5 the transmission and reflection coefficients for both situations are shown. It can be seen that the frequency of the transmission notch changes from 1.85 GHz to 1.63 GHz when the sensor is covered with the material. This frequency shift allows the detection of the covering material and the estimation of the real part of its permittivity. Therefore, the resonant frequency of the SRRs depends on the material covering the sensor, which can be used for sensing purposes.

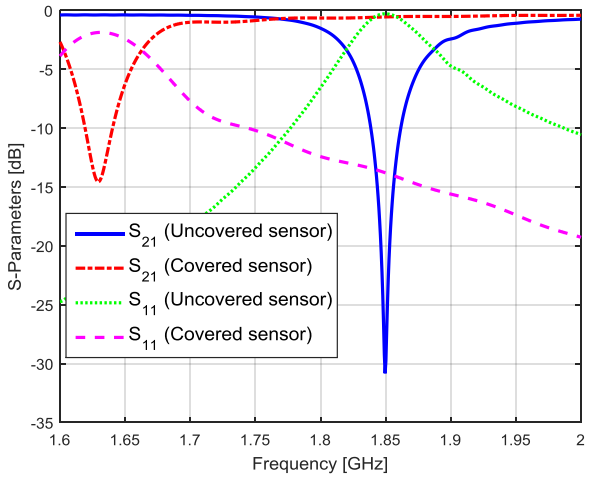

Fig. 5. Simulated S-parameters of the uncovered and covered sensors.

III. Dielectric Characterization of Solids

In order to obtain the response of the sensor when sensing solid materials, some materials with different electromagnetic characteristics have been chosen. These solids are shown in TABLE I. In all of the cases, the thickness of the solids is over $0.1\lambda_g$, which is a value large enough to be in the optimal sensing zone for the characterization of solids (as it will be demonstrated later in Section IV). Thus, this parameter does not affect the notch frequency and the sensor can be used to estimate the complex permittivity of the solids.

First of all, the solids have been characterized by using the Agilent Verification Kit 85055A. These measurements are destructive, because a sample of the MUT must be fitted into a 50-Ω coaxial line with specific dimensions. The obtained values for the characterization are shown in TABLE I, where can be noticed that the real part of the complex permittivity (ε'_r) of the selected samples is between 1.05 and 3.85, while the imaginary part (ε''_r) is between 0.0018 and 0.0828.

TABLE I
Relative Permittivity of the Solid Materials Measured with the 85055A Verification Kit

Material	Real part of the relative permittivity (ε'_r)	Imaginary part of the relative permittivity (ε''_r)	Tangent loss ($tan\ \delta$)
Foam	1.05	0.0018	0.0017
High Density Foam	1.78	0.0294	0.0165
Polyethylene	2.08	0.0287	0.0138
FR4	3.85	0.0828	0.0215

Then, the response of the sensor covered with different materials has been simulated by using ADS ®. The solids have been simulated considering the dielectric characteristics obtained with the verification kit. Fig. 6 shows the dependency of the complex permittivity on the frequency shift in % (with respect to the resonant frequency of the sensor in vacuum) when detecting each material. It can be observed that, for the analyzed samples, the frequency variation changes between 0.27% and 9.61% for a relative permittivity variation between 1.05 and 3.85. Thus, an expression which approximates the simulated response of the sensor is given by

$$\Delta f_{approx}\,[\%] = \frac{\max(\Delta f\,[\%])}{2\cdot\sqrt[4]{\max(\varepsilon'_r)}}\cdot\varepsilon'_r - \frac{4}{9}\cdot\frac{\max(\Delta f\,[\%])}{\sqrt[4]{\max(\varepsilon'_r)}} - \frac{28}{100} \quad (7)$$

where $max(\Delta f[\%])$ = 9.61% and $max(\varepsilon'_r)$ = 3.85 are the maximum frequency shift obtained and the maximum relative permittivity used to fit the curve, respectively. The mean error between the simulated and fitted curves is 6.79%, while between the measurements and the fitted curves is 10.42%.

The previous approximation can be used to easily estimate ε'_r after the measurement of the shift in frequency ($\Delta f_{meas}[\%]$) produced by a sample when covering the sensor:

$$\varepsilon'_r = 2\cdot\sqrt[4]{\max(\varepsilon'_r)}\cdot\Delta f_{meas}[\%] + \frac{8}{9}\cdot\max(\Delta f[\%]) + \frac{14}{25}\cdot\sqrt[4]{\max(\varepsilon'_r)} \quad (8)$$

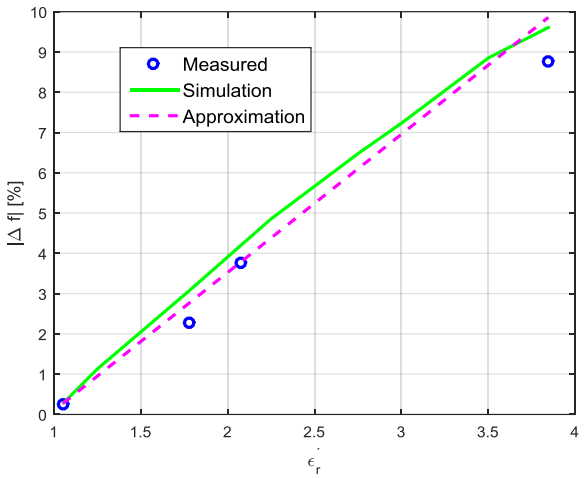

Fig. 6. Frequency shift depending on the relative permittivity of the solids: measured (blue dots), simulated (solid green) and approximated (dashed magenta).

The sensitivity of the sensor can be defined as the measured frequency shift in the transmission notch with respect to the uncovered sensor (in %) over the shift of the real part of the complex permittivity, $\Delta f\ [\%]/\Delta\varepsilon'$, resulting in 3.04 %. This gives a figure of merit of the proposed sensor, so it can be compared with other approaches.

Finally, samples of the solid materials in Table I have been used to cover the prototype. The measured frequency shifts in the transmission notch with respect to the uncovered sensor are also plotted in Fig. 6. The values obtained with the characterization kit have been considered for the relative permittivity of each sample. There is a good agreement between simulations and measurements and the trend is similar. However, there are some differences caused by errors produced when measuring the permittivity with the dielectric characterization kit. Also there are air gaps when covering the sensor with some samples.

In TABLE II the results of the shift on the magnitude of s_{21} between the uncovered and covered sensor are shown. It can be seen that the mean displacement is 4.35%. Thus, an expression which estimates the imaginary part of the complex permittivity of the MUT is given by

$$\varepsilon'' = -0.4501 \cdot \Delta|s_{21}|^2 + 1.3269 \cdot \Delta|s_{21}| - 0.8959 \quad (9)$$

where $\Delta|s_{21}|$ corresponds to the shift of the magnitude of s_{21} between the uncovered and covered sensor. The mean error obtained between the approximation (9) and the measurements is 6.89%. The estimation of ε'' is not linear. Thus, the sensitivity cannot be defined for this measurement.

TABLE II
TRANSMISSION COEFFICIENT SHIFT FOR THE CHARACTERIZATION OF THE IMAGINARY PART OF THE PERMITTIVITY IN SOLIDS

Material	Measured $\Delta\|s_{21}\|$	Simulated $\Delta\|s_{21}\|$	Displacement [%]
Foam	1.0519	1.0388	1.25
High Density Foam	1.1157	1.2205	8.59
Polyethylene	1.1389	1.2294	7.36
FR4	1.4607	1.4577	0.21

IV. THIN-FILM DETECTION

In this section it is shown that the sensor is capable of detecting the thickness of thin-films. Both, simulations and measurements are shown.

The first study that is presented is the effect of the protection layer that is used on the sensor for submersible applications. To do this, a comparison between the sensor with and without the protection layer has been carried out.

Second, simulations of the sensor covered with three materials are presented. Each material has a different complex permittivity and the sensor is characterized by changing the thickness of each material. Those simulations show the behavior of the sensor when detecting thickness and let to obtain the maximum detectable thickness.

In third place, the simulations are compared with the measurements of different materials in order to corroborate the behavior previously obtained with the simulations. Moreover, the viability of the sensor in practical applications is also demonstrated.

A. Protection layer effect

The proposed protection consists on an 80-μm thin-film layer of a plastic material (ImageLast from Fellowes ®). This thin-film layer is added to the sensor through the commercial laminator machine *Photopro 33* of the company Albyco Nederland B.V. by heating the plastics. In this section, the behavior of this protection is studied. As it has been said, the sensor is proposed to be submersible and reusable, thus, in Section V all measurements will be done after protecting the sensor with this method.

The effect of the protection layer is shown in Fig. 7, where the frequency response of the transmission coefficient is shown for the unprotected and protected sensors. It can be observed that both responses are similar, but there is a 30 MHz frequency shift (1.63% with respect to the unprotected sensor frequency) towards lower frequencies for the case of the protected sensor. This is produced because of the change in the real part of the complex permittivity due to the addition of the protection layer, as explained in Section II. This result shows the ability of the sensor to detect film layers placed over its surface.

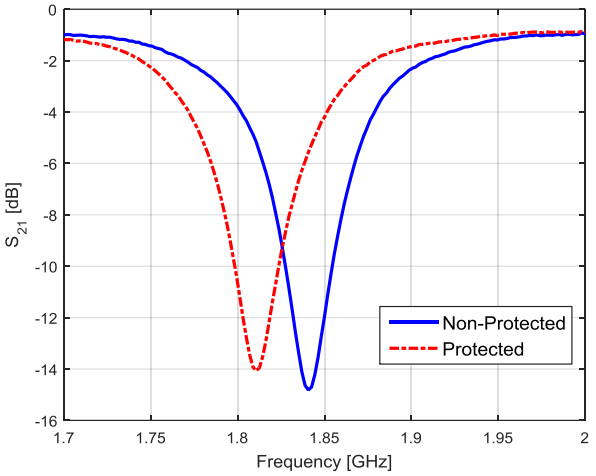

Fig. 7. Measured transmission coefficient of the unprotected and protected sensors.

B. *Material thickness: simulations*

In Fig. 8 the simulations for three different materials (ε_r' = 3.5, 5 and 7) placed over the sensor are shown. The simulations have been performed with the software ADS (Advanced Design System) ®. A parametric study of the transmission notch frequency with material thickness is presented. The material thickness in terms of the uncovered microstrip guided resonance wavelength, λ_g, is represented in the x-axis, while the frequency shift from the resonant frequency of the unloaded sensor, in %, is represented in the y-axis.

The sensor presents the same behavior for all the loading materials. First, there is a region where the resonant frequency changes with thickness. Then, there is a region where the resonant frequency becomes constant. Thus, for thickness sensing application it is required to work in the first region, while for materials characterization the second region will be used. This effect is related to the explanation in Section II, where it was explained that the effective permittivity increases with increasing covering material thickness. This is true up to a maximum thickness value. Over that value, the field lines are concentrated within the sensor substrate and the covering material and the effective permittivity does not change, leading to a constant resonant frequency. The saturation point is defined as the maximum thickness considered for thin-film sensing applications. In this study it is considered that the saturation point is 10% of the constant frequency in the saturation region. The saturation point is $t/\lambda_g \approx 0.02$ independently of the covering material.

Fig. 8 shows the dependence of the frequency shift with the relative permittivity of the material. For a material with ε_r' = 3.5, the frequency shift goes from 1.62% to 8.70%, while for a material with ε_r' = 5 goes from 2.11% to 12.70% and for ε_r' = 7 goes from 2.70% to 17.35%. Moreover, the sensitivity is not the same in the entire sensing region. The sensitivity is maximum between $t/\lambda_g \approx 2\cdot10^{-3}$ and $t/\lambda_g \approx 2\cdot10^{-2}$, where a linear approximation can be considered:

$$\Delta f\ [\%] = 1.3 \cdot \varepsilon_r \cdot \left(t/\lambda_g\right) + 4.5 \cdot \varepsilon_r \qquad (10)$$

This allows obtaining the thickness of a thin film once the permittivity of the material and the frequency shift are known.

In Fig. 8 the linear approximation for each MUT is also plotted. The mean error between the approximation and the simulation is 2.23% for the material of ε_r' = 3.5, 2.83% for ε_r' = 5 and 3.58% for ε_r' = 7.

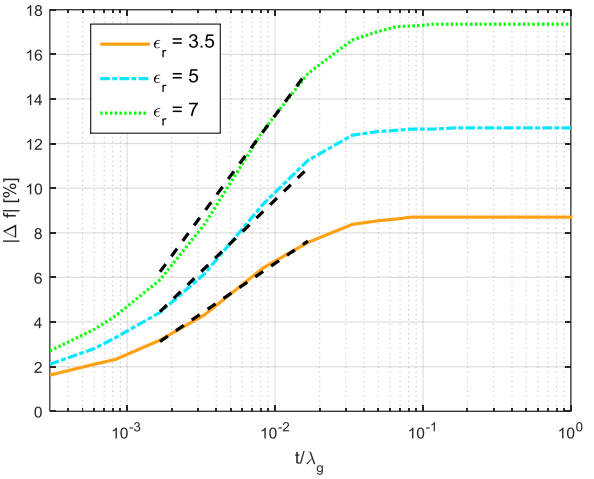

Fig. 8. Frequency shift depending on the thickness of a material with ε_r'=3.5, 5, and 7. The dashed black lines are the approximations for the linear sensing region.

The sensitivity of the proposed sensor for thin-film applications is defined as the measured frequency shift in the transmission notch with respect to the uncovered sensor (in %) over the increment in the material thickness situated over the sensor, *Δf [%]/Δt [mm]*. This magnitude is proportional to ε_r'. If this definition of the sensitivity is normalized to the value of ε_r' results in a constant value equal to 1.43 %/mm.

C. *Material thickness: measurements*

In this subsection the behavior of the sensor when it is covered with two different materials is analyzed. The materials have been chosen due to their thin thickness. They are 80-grams paper sheets with a thickness of 100 µm and plastics films with 80-µm thickness. The plastic films are the same than the used for protecting the sensor.

First of all, a set of simulations and measurements has been performed in order to estimate the real part of the complex permittivity of those materials. For that purpose, the frequency shift between the notch frequency of the covered and uncovered sensors have been computed and measured. The frequency shift obtained between the paper-covered and the uncovered sensors corresponds to 78.10 MHz. This value is 88.10 MHz for the case of the plastic-loaded sensor. Thus, the paper presents a real part of the relative permittivity of 2.06, while it is 2.19 for the case of the plastic. Fig. 9 shows the transmission coefficient ($|s_{21}|$) of the fabricated sensor for all the covered and uncovered cases. In all of the cases the transmission coefficient is shown for thickness values that do not affect the response of the sensor. Thus, the resonant

frequency does not depend on the thickness of the covering material.

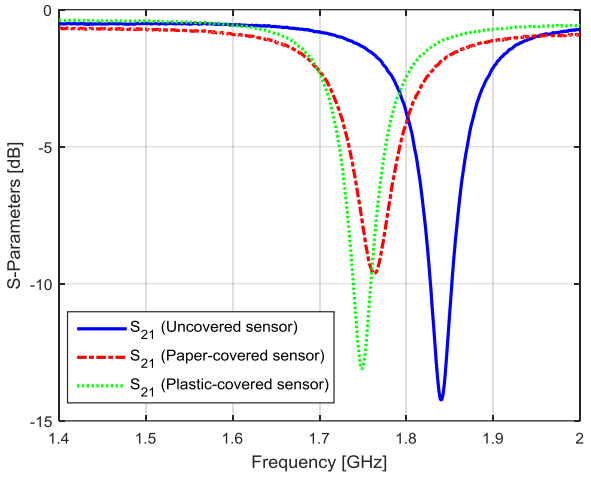

Fig. 9. Measured transmission coefficient of fabricated sensor for uncovered case (solid blue) and the paper-covered (dashed red) and plastic-covered (dotted green) cases when the sensor is saturated.

Fig. 10 and Fig. 11 show the simulations and measurements for the sensor covered with paper and plastic, respectively. The x-axis represents the thickness of the material, while the frequency shift with respect to the resonant frequency of the uncovered sensor is represented in the y-axis. Measurements and simulations have been performed with a thickness variation from t = 100 µm to 50.1 mm for the paper, and from t = 80 µm to 13.92 mm for the plastic.

From Fig. 10 (sensor covered with paper) it can be seen that the thickness sensing region in this case follows a linear relation. This is due to the fact that the measurements start with a thickness of 100 µm, which is within the linear zone of the sensing region. In the figure, it can be seen that the frequency shift for measurements varies from 1.53% to 4.24%, while for simulations varies from 1.61% to 4.24%. There is a good agreement between the measurements and simulations along all the thickness variation. The saturation point, $t/\lambda_g \approx 0.02$, is approximately the same for the simulations and measurements. A linear approximation which defines the sensing region for the measurements is given by

$$\Delta f\ [\%] = 2.3345t + 3.9555 \qquad (11)$$

where the parameter t is measured in mm. The mean error between the approximated curve and the measurements is 3.10%.

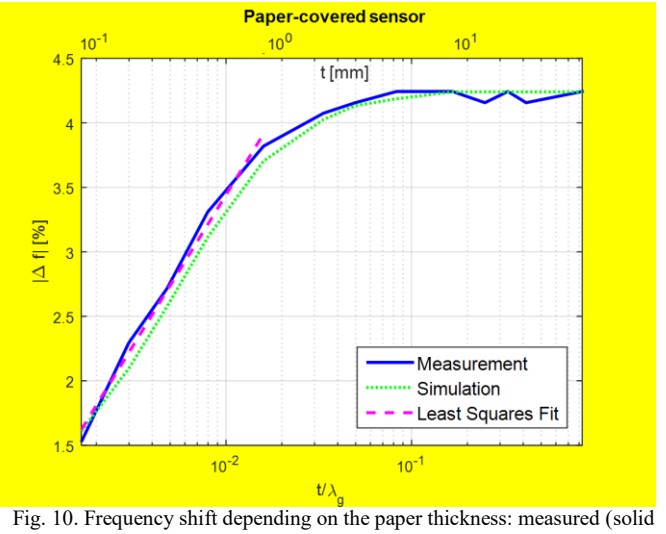

Fig. 10. Frequency shift depending on the paper thickness: measured (solid blue), simulated (dotted green), least squares fit for the sensing region (dashed magenta).

Fig. 11 shows the results for the plastic films. The thickness sensing region is also defined by a linear relation. There is a good agreement between simulations and measurements. In the figure can be seen as the frequency shift for measurements varies from 1.23% to 4.72%, while for simulations varies from 1.61% to 4.72%. The saturation point for both, measurements and simulations is the same: $t/\lambda_g \approx 0.02$. The expression which approximates the sensing region for the measurements is given by

$$\Delta f\ [\%] = 2.5971t + 11.8486 \qquad (7)$$

and has been computed through least squares fitting, where the parameter t is measured in mm. The mean error between the linear approximation and the measurements is 2.51%.

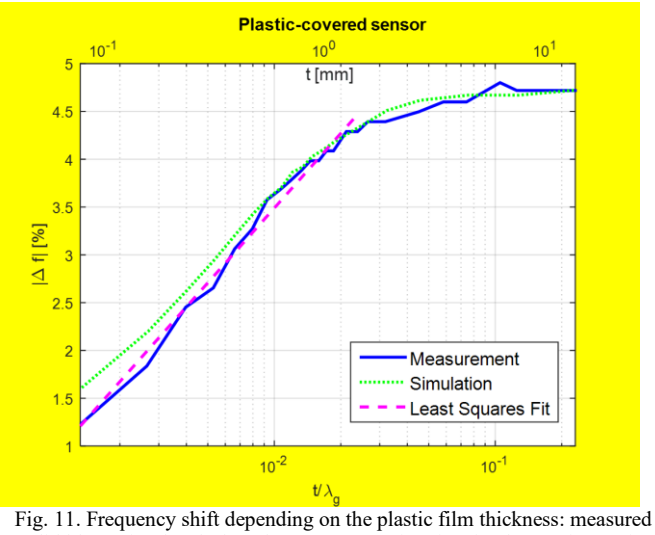

Fig. 11. Frequency shift depending on the plastic film thickness: measured (solid blue), simulated (dotted green), approximation for the sensing region (dashed magenta).

Therefore, it can be seen that the sensor is suitable for the measurement of thin films. This has been corroborated with simulations and measurements.

V. Dielectric Characterization of Liquids

In order to obtain the response of the sensor when sensing liquid materials, some liquids with different electromagnetic characteristics have been chosen. These liquids are shown in TABLE III.

First of all, the liquids have been characterized by using the Agilent 85070E Dielectric Probe Kit at room temperature. These measurements are non-destructive, because they are made by just immersing the probe into the liquids. The obtained values for the characterization are shown in TABLE III, where it can be noticed that the real part of the relative permittivity (ε_r') of the selected samples is between 2.45 and 22.52, while the imaginary part of the relative permittivity (ε_r'') is between 0.0387 and 0.9391.

TABLE III
Relative permittivity of the liquids measured with the characterization dielectric probe kit 85070E

Material	Real part of the relative permittivity (ε_r')	Imaginary part of the relative permittivity (ε_r'')	Tangent loss ($tan\ \delta$)
Paraffin Oil	2.45	0.0387	0.0158
Olive Oil	2.94	0.2540	0.0864
Peanut Oil	2.94	0.2555	0.0869
Almond Oil	2.96	0.2623	0.0886
Soy Oil	3.00	0.2835	0.0945
Lemon Oil	3.03	0.2145	0.0708
Castor Oil	3.37	0.3865	0.1147
Chloroform	5.77	0.3145	0.0545
Acetone	22.52	0.9391	0.0417

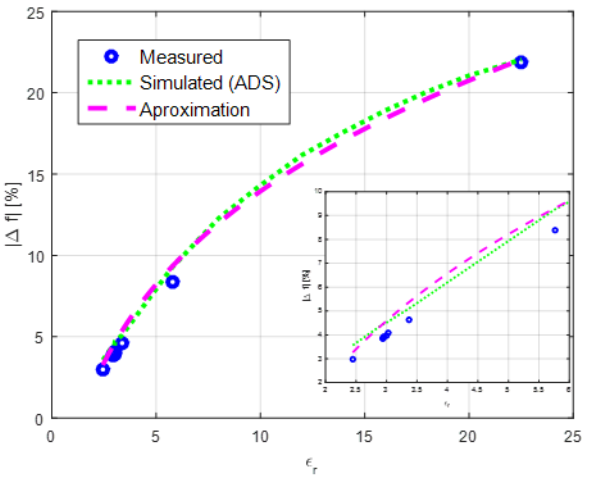

Fig. 12. Frequency shift depending on the real part of the relative permittivity of the liquids: measured (blue dots), simulated (dotted green) and approximated (dashed magenta). The inset shows the range between ε_r = 2.45 and 5.77.

Then, the response of the sensor immersed in the different liquids has been simulated by using ADS ®. The liquids have been simulated considering the electromagnetic characteristics obtained with the dielectric characterization kit. Fig. 12 shows the dependency of the real part of the relative permittivity on the frequency shift in % (with respect to the resonant frequency of the sensor in vacuum) when detecting each liquid. It can be observed that, for the analyzed samples, the frequency variation changes between 2.98% and 21.9% for a real part of the relative permittivity variation between 2.45 and 22.52. As can be noticed, in the presented results, there is a large gap, in terms of permittivity, between the last liquid (ε_r' = 22.52) and the previous one (ε_r'= 5.77). This was due to the impossibility to find non-polar liquids with relative permittivity between these values. In order to obtain a characteristic curve that fits the behavior of the liquids, additional simulations have been taken into account within that range. From the equations (3) and (4) it can be deduced the expression

$$f_o = \frac{1}{\pi} \cdot \sqrt{\frac{c \cdot Z_o}{L \cdot p}} \cdot \frac{1}{\sqrt[4]{\varepsilon_{eff}}} \tag{12}$$

where it can be seen that the resonant frequency has a dependence of a fourth root factor with the effective permittivity. It can be seen in (2) that the relation between the effective and relative permittivities for the microstrip technology is linear. Thus, an expression which approximates the simulated frequency shift response of the sensor is given by

$$\Delta f_{approx}[\%] = \frac{\max(\Delta f[\%]) \cdot 2}{\sqrt[4]{\max(\varepsilon_r')}} \cdot \sqrt[4]{\varepsilon_r'} - \max(\Delta f[\%]) \tag{13}$$

where $max(\Delta f[\%])$ = 22.04% and $max(\varepsilon_r')$ = 22.52 are the maximum frequency shift obtained and the maximum relative permittivity used to fit the curve, respectively. The mean error between the simulated and fitted curves is 2.37%, while between the measurements and the fitted curves is 7.83%.

The previous approximation can be used to easily estimate ε_r' after the measurement of the shift in frequency ($\Delta f_{meas}[\%]$) produced when immersing the sensor:

$$\varepsilon_r' = \left[\frac{\Delta f_{meas}[\%] + \max(\Delta f[\%])}{\max(\Delta f[\%]) \cdot 2}\right]^4 \cdot \max(\varepsilon_r') \tag{14}$$

In TABLE II the results of the shift on the magnitude of the transmission coefficient between the uncovered and immersed sensor are shown. It can be seen that the mean displacement is 4.35%. Thus, an expression which estimates the imaginary part of the complex permittivity of the liquid under test is given by

$$\varepsilon'' = 0.5489 \cdot \Delta|s_{21}|^2 - 0.9423 \cdot \Delta|s_{21}| + 0.4264 \tag{15}$$

where $\Delta|s_{21}|$ corresponds to the shift in the magnitude of transmission between the unloaded and submerged sensor. The mean error obtained between the approximation (15) and the measurements is 8.34%.

TABLE IV
TRANSMISSION COEFFICIENT SHIFT FOR THE CHARACTERIZATION OF THE IMAGINARY PART OF THE PERMITTIVITY IN LIQUIDS

Material	Measured $\Delta\|s_{21}\|$	Simulated $\Delta\|s_{21}\|$	Displacement [%]
Paraffin Oil	1.033	1.0236	0.91
Olive Oil	1.4811	1.4932	0.82
Peanut Oil	1.4675	1.5158	3.29
Almond Oil	1.5052	1.5263	1.40
Soy Oil	1.5296	1.5636	2.22
Lemon Oil	1.3838	1.4277	3.17
Castor Oil	1.7441	1.7145	1.70
Chloroform	1.5545	1.6279	4.73
Acetone	2.1384	1.8842	11.89

The liquid measurements have been performed by immersing the SRRs of the sensor in the different sample liquids at room temperature, as shown in Fig. 13. In order to make the sensor reusable, the protection technique presented in Section IV.A has been used. It is noteworthy that the frequency response of the sensor returns quickly to its initial state once the sensor is removed from the liquid and the possible residuals are properly eliminated. This can be done by using a solvent like acetone. The response of the sensor when immersed in the different liquids is shown in Fig. 12. The frequency shift caused by the immersion in each liquid is associated to the corresponding ε_r' previously obtained with the dielectric probe kit, while variation in the s_{21} magnitude is associated to ε_r''. There is a good agreement between simulation and measurements. The mismatch between simulations and measurements is mainly due to the error [35] introduced when measuring the complex permittivity of the liquids with the dielectric probe kit.

Fig. 13. Sensor immersed in olive oil.

VI. CONCLUSIONS

A Split-Ring Resonator-based sensor for dielectric characterization of solids and liquids has been proposed. This sensor is based on the frequency shift of the notch, introduced in the transmission coefficient, when a solid is placed over the structure or when it is immersed in different liquids. This is used to obtain the permittivity of solids and liquids. Moreover, it has been found that the frequency shift is constant when the thickness of the material placed over the sensor is over $0.1\lambda_g$. Below this value, the frequency shift of the transmission coefficient depends on the thickness of the covering material. In that situation, the sensor can be used as an effective thin-film thickness detector.

This work has been focused on the design, fabrication and validation of the sensor for different applications: the determination of the thickness materials and the dielectric characterization of solid and liquid materials. Simulations and measurements have been performed, obtaining good matching. It is important to note that this sensing technique is non-destructive.

Hence, a completely passive, low-cost and low-complexity fabrication sensor has been presented and validated. Furthermore, the sensor presents real-time response and high sensitivity, which makes the proposed sensor a good candidate for the proposed applications. Finally, it has been demonstrated that the sensor can be easily protected for liquids immersion, obtaining a fully submersible and reusable sensor. These characteristics make the proposed sensor very competitive with existing technologies. Making a further comparison with the standard kits, the characterization kit for the solid materials is based on a destructive method, while the proposed approach is non-destructive. It can be seen from the technical overview of the dielectric probe kit for liquids characterization [35] that the equipment is not recommended for low loss ($\tan\delta < 0.5$) materials with $\varepsilon_r' > 5$. This limitation is not present with the proposed approach. Moreover, TABLE V compares the proposed sensor with the other SRR-based sensors found in literature. The proposed approach presents a clear advantage over other devices, because the same device can be used for solids and liquids dielectric characterization and thin film measurements. Other works are only focused on one of the three covered topics. Even the commercial characterization probes for network analyzers are focused on liquids or solids, but they do not perform measurements on both. Finally, the proposed sensor is the only one that is fully submersible and reusable.

As a future improvement, it would be interesting to develop a version of the sensor based on SRRs with different resonance frequencies, in order to determine the complex permittivity and the thickness of solids at the same time.

TABLE V
STATE OF THE ART

Approach	Solids char.	Liquids char.	$\frac{\Delta f[\%]}{\Delta\varepsilon'}$	Thin-film detection	Submersible
[1]	No	Yes	5.89%	No	No
[19]	Yes	No	2.90%	No	No
[21]	No	No	-	Yes	No
[22]	No	No	-	Yes	No

[23]	No	No	-	Yes	No
[24]	No	Yes	0.15%	No	No
[27]	No	Yes	0.02%	No	No
[28]	No	Yes	0.46%	No	No
[29]	No	Yes	0.11%	No	No
Proposed Sensor	Yes	Yes	3.04%	Yes	Yes

ACKNOWLEDGMENT

The authors want to thank Dr. Javier Pozuelo de Diego for his support during the characterization of the solid and liquid materials.

REFERENCES

[1] S. Kulkarni, and M. S. Joshi, "Design and Analysis of Shielded Vertically Stacked Ring Resonator as Complex Permittivity Sensor for Petroleum Oils", *IEEE Transactions on Microwave Theory and Techniques*, vol. 63, no. 8, August 2015.

[2] M. T. Jilani, M. Z. Rehman, A. M. Khan, M. T. Khan, and S. M. Ali, "A Brief Review of Measuring Techniques for Characterization of Dielectric Materials", *ITEE Journal*, vol. 1, no. 1, December 2012.

[3] A. P. Gregory, and R. N. Clarke, "A Review of RF and Microwave Techniques for Dielectric Measurements on Polar Liquids," *IEEE Transactions on Dielectrics and Electrical Insulation*, vol. 13, no.4, August 2006.

[4] F. Martín, "Metamaterials for Wireless Communications, Radiofrequency Identification, and Sensors", *ISRN Electronics*, vol. 13, no. 3, 2012.

[5] E. M. Amin, J. K. Saha, and N. C. Karmakar, "Smart Sensing Materials for Low-Cost Chipless RFID Sensor," *IEEE Sensors Journal*, vol. 14, no. 7, July 2014.

[6] E. M. Amin, and N. C. Karmakar, "Development of a chipless RFID temperature sensor using cascaded spiral resonators," *Sensors 2011*.

[7] T. Chen, S. Li, and H. Sun, "Metamaterials Application in Sensing," *Sensors*, vol. 12, no. 3, pp. 2742-2765, 2012.

[8] M. N. Jaric, S. F. Romanuik, G.A. Ferrier, G.E. Bridges, M. Butler, K. Sunley, D. J. Thomson, and M. R. Freeman, "Microwave frequency sensor for detection of biological cells in microfluidic channels," *Biomicrofluidics*, vol. 3, no. 3, 2009.

[9] B. R. Jean, C. G. Eric, and J. M. Melanie, "A microwave frequency sensor for non-invasive blood-glucose measurement," *Sensors Applications Symposium, 2008. SAS 2008. IEEE*. IEEE, 2008.

[10] F. M. Battiston, J.P. Ramseyer, H. P. Lang, M. K. Baller, Ch. Gerber, J. K. Gimzweski, E. Meyer, and H. J. Güntherodt, "A chemical sensor based on a microfabricated cantilever array with simultaneous resonance-frequency and bending readout," *Sensors and Actuators B: Chemical*, vol. 77, no. 1, p 122-131, 2001.

[11] H. J. Lee, H. S. Lee, K. H. Yoo, and J. G. Yook, "DNA sensing using split-ring resonator alone at microwave regime," *Journal of Applied Physics*, vol. 108, no. 1, 2010.

[12] M. Yoo, H. K. Kim, and S. Lim, "Electromagnetic-based ethanol chemical sensor using metamaterial absorber", *Sensors and Actuators*, vol. 222, pp. 173-180, January 2016.

[13] Y. Sujan, B. Vasuki, G. Uma, D. Ezhilarasi, and K. Suresh, "Thickness Sensor for Ferromagnetic Sheets," *International Conference on Sensing Technology (ICST)*, pp. 93-96, 2012.

[14] H.C. Wang, A. Zyuzin, and A. V. Mamishev, "Measurement of Coating Thickness and Loading Using Concentric Fringing Electric Field Sensors," *Sensors Journal*, vol. 14, no. 1, pp. 68-78, 2014.

[15] J. B. Pendry, A. J. Holden, D. J. Robbins, and W. J. Stewart, "Magnetism from Conductors and Enhanced Nonlinear Phenomena," *IEEE Transactions on Microwave Theory and Techniques*, vol. 47, no. 11, November 1999.

[16] M. Schüßler, C. Mandel, M. Puentes, and R. Jakoby, "Metamaterial Inspired Microwave Sensors," *IEEE Microwave Magazine*, vol. 13, pp. 57-68, 2012.

[17] J. Naqui, and F. Martin, "Transmission Lines Loaded With Bisymmetric Resonators and Their Application to Angular Displacement and Velocity Sensors," *IEEE Transactions on Microwave Theory and Techniques*, vol. 61, no. 12, pp. 4700-4716, December 2013.

[18] J. Naqui, J. Coromina, F. Martin, A. K. Horestani, and C. Fumeaux, "Comparative Analysis of Split Ring Resonators (SRR), Electric-LC (ELC) Resonators, and S-Shaped Split Ring Resonators (S-SRR): Potential application to rotation sensors," *Microwave Symposium (MMS)*, pp. 1-5, 2014.

[19] C. S. Lee, and C. L. Yang, "Complementary Split-Ring Resonators for Measuring Dielectric Constants and Loss Tangents," *IEEE Microwave and Wireless Components Letters*, vol. 24, no. 8, pp. 563-565, August 2014.

[20] J. Naqui, M. Durán-Sindreu, and F. Martín, "Novel sensors based on the symmetry properties of split ring resonators (SRRs)," *Sensors*, vol. 11, no. 8, pp. 7545-7553, 2011.

[21] J. F. O'Hara, R. Singh, I. Brener, E. Smirnova, J. Han, A. J. Taylor, and W. Zhang, "Thin-film sensing with planar terahertz metamaterials: sensitivity and limitations," *Optics Express*, vol. 16, no. 3, 2008.

[22] A. Elhawil, J. Stiens, C. De Tandt, W. Ranson, and R. Vounckx, "Thin-film sensing using circular split-ring resonator at mm-wave frequencies," *Applied physics A*, vol. 103, no. 3, 2011.

[23] X. J. He, L. Qiu, Y. Wang, Z. Geng, J. Wang, and T. Gui, "A Compact Thin-Film Sensor Based on Nested Split-Ring-Resonator (SRR) Metamaterials for Microwave Applications," *Journal of infrared, millimeter and terahertz waves*, vol. 32, no. 7, 2011.

[24] W. Withayachumnankul, K. Jaruwongrungsee, A. Tuantranont, C. Fumeaux, and D. Abbott, "Metamaterial-based microfluidic sensor for dielectric characterization",*Sensors and actuators,* vol. 189, pp. 233-237, January 2013.

[25] T. Chen, D. Dubuc, M. Poupot, J. J. Fournié, and K. Grenier, "Accurate Nanoliter Liquid Characterization Up to 40 GHz for Biomedical Applications: Toward Noninvasive Living Cells Monitoring," *IEEE Transactions on Microwave and Techniques*, vol. 60, no. 12, pp. 4171-4177, December 2012.

[26] K. Grenier, D. Dubuc, P. E. Poleni, M. Kumemura, H. Toshiyoshi, T. Fujii, and H. Fujita, "Integrated Broadband Microwave and Microfluidic Sensor Dedicated to Bioengineering," *IEEE Transactions on Microwave Theory and Techniques*, vol. 57, no. 12, pp. 3246-3253, December 2009.

[27] A. A. Abduljabar, D. J. Rowe, A. Porch, and D. A. Barrow, "Novel Microwave Microfluidic Sensor Using a Microstrip Split-Ring Resonator," *IEEE Transactions on Microwave Theory and Techniques*, vol. 62, no. 3, pp. 679-688, March 2014.

[28] A. Ebrahimi, W. Withayachumnankul, S. Al-Sarawi, and D. Abbott, "High-Sensitivity Metamaterial-Inspired Sensor for Microfluidic Dielectric Characterization," *IEEE Sensors Journal*, vol. 14, no. 5, pp. 1345-1351, May 2014.

[29] D. J. Rowe, S. al-Malki, A. A. Abduljabar, A. Porch, D. A. Barrow, and C. J. Allender, "Improved Split-Ring Resonator for Microfluidic Sensing", *IEEE Transactions on Microwave Theory and Techniques*, vol. 62, no. 3, March 2014.

[30] R. Marqués, F. Martín, and M. Sorolla, "Metamaterials with Negative Parameters: Theory, Design and Microwave Applications". Hoboken, NJ, USA: IEEE-Wiley, 2008.

[31] K.C. Gupta, R. Garg, I. Bahl, and P. Bhartia, "Microstrip Lines and Slotlines" (2nd edition), Boston Artech House, 1996.

[32] I. J. Bahl, and S. S. Stuchly, "Analysis of a Microstrip Covered with a Lossy Dielectric," *IEEE Transaction on Microwave Theory and Techniques*, vol. MTT-28, no.2, February 1980.

[33] J. Svacina, "Analysis of Multilayer Microstrip Lines by a Conformal Mapping Method," *IEEE Transactions on Microwave Theory and Techniques*, vol. 40, no. 4, April 1992.

[34] I. J. Bahl, and P. Bhartia, "Microwave solid state circuit design". Wiley New York, 1988.

[35] "Keysight 85070E Dielectric Probe Kit, 200 MHz to 50 GHz – Technical Overview," Keysight Technologies, USA, August, 2014.